

Numerical continuation of families of homoclinic connections of periodic orbits in the RTBP

E. Barrabés*, J.M. Mondelo†, M. Ollé‡

March 16, 2009

Abstract

The goal of this paper is the numerical computation and continuation of families of homoclinic connections of the Lyapunov families of periodic orbits (p.o.) associated with the collinear equilibrium points, L_1 , L_2 and L_3 , of the planar circular Restricted Three–Body Problem (RTBP). We describe the method used that allows to follow individual families of homoclinic connections by numerical continuation of a system of (nonlinear) equations that has as unknowns the initial condition of the p.o., the linear approximation of its stable and unstable manifolds, and a point in a given Poincaré section in which the unstable and stable manifolds match. For the L_3 case, some comments are made on the geometry of the manifold tubes and the possibility of obtaining trajectories with prescribed itineraries.

Keywords: periodic orbits, invariant manifolds, homoclinic connections, numerical methods, Restricted Three–Body Problem.

1 Introduction

Homoclinic and heteroclinic connections of hyperbolic objects play an important role in the study of dynamical systems from a global point of view.

*Dept. Informàtica i Matemàtica Aplicada. Universitat de Girona, Avda. Lluís Santaló s/n, 17071 Girona, Spain. (barrabes@ima.udg.edu).

†IEEC & Dept. Matemàtiques. Universitat Autònoma de Barcelona, Edifici C, 08193 Bellaterra, Spain. (jmm@mat.uab.es).

‡Dept. de Matemàtica Aplicada I. Universitat Politècnica de Catalunya, Diagonal 647, 08028 Barcelona, Spain. (merce.olle@upc.edu).

Of special interest is their application to the design of space missions using Libration Point dynamics. Since 1978, when NASA launched the ISEE-3 spacecraft, Lissajous and Halo type trajectories around the collinear equilibrium points have been considered in the trajectory design of space missions. Most Libration Point missions launched up to present [14] consist essentially of a single nominal trajectory and a transfer trajectory to it. The Genesis mission [25] has been the first one to make use of an heteroclinic connection. The use of homoclinic and heteroclinic phenomena allows to envisage more complex missions, like low-energy transfers to the Moon [37] and the *Petit Grand Tour* to the moons of Jupiter [21]. Having as a goal the design of such complex missions in a systematic way, it is desirable to construct maps of homoclinic and heteroclinic connections in several primary-secondary systems. The methodology developed in this paper is mostly aimed to the construction of such maps.

The Circular Restricted Three-Body Problem (RTBP) is the natural problem to start with when analyzing such space missions. Attention is mostly focused on L_1 and L_2 , because of its suitability to place permanent observatories of the Sun or of the whole celestial sphere (like WMAP, around L_2 , see [14] for a short description of both this mission and SOHO). Analytical proofs of the existence of homoclinic orbits to Lyapunov periodic orbits (LPO) around the L_1 and L_2 points have been given in [32], for some particularly shaped homoclinic orbits, and in [30], where the authors considered the homoclinic connections of LPO around L_1 (L_2 in that paper) for values of the mass parameter μ close to 0 and values of the Jacobi constant, C , close to the one at L_1 . More recently, and by means of a computed assisted proof approach (see [40, 41]), proofs have been given of the existence of particularly shaped homoclinic and heteroclinic connections of Lyapunov orbits around L_1 and L_2 , for the particular value of $\mu = 0.00095387$ (the mass parameter value for the Oterma comet in the Sun-Jupiter system) and the Jacobi constant $C = 3.03$.

From a numerical point of view, families of homoclinic and heteroclinic connections of periodic and quasi-periodic solutions around L_1 and L_2 have been computed in the literature by means of the use of semi-analytical techniques, in order to compute the families of invariant objects to connect and its stable and unstable invariant manifolds. After that, individual connections are found by matching the corresponding manifolds on a surface of section. Families are described by repeating this matching process for several values of a parameter, which is often the energy (or equivalently the Jacobi constant). This approach has been successfully applied in many situations, [8, 21, 22, 23, 27]. However, there is the possibility to improve

it in some aspects. Semi-analytical techniques are very accurate near an equilibrium point, but lose accuracy as we get away from it. In some situations (like the L_3 point of the circular Restricted Three-Body Problem), they do not give useful approximations at all [26]. Moreover, in the case of d -dimensional invariant tori for $d \geq 2$, the manifold matching process can be time consuming, since a d -dimensional parameter space needs to be scanned. It would be desirable to use numerical methodology for the continuation of individual families of connections.

From a theoretical point of view, a suitable Poincaré section would reduce the problem of computation and continuation of homoclinic connections of p.o. to the computation and continuation of homoclinic connections of fixed points of maps. Numerical methodology for this has been developed in [5, 42]. This approach is not practical in our setting, due to the complicated geometry of the manifold tubes (see Sect. 3.2), which makes difficult to find an explicit expression of a Poincaré section valid throughout the connection. Therefore, it is needed to work directly in the ODEs.

In the computations of this paper, we have used a method for the continuation of homoclinic connections that consists of raising a (nonlinear) system of equations whose solution is a curve that corresponds to a family of homoclinic connections. This systems includes the equations of a p.o. in a Poincaré section, the eigenvalue/eigenvector equations for the linear approximation of the invariant manifolds of the p.o., and matching conditions for the manifolds on another Poincaré section. Such quantities are numerically continued using a predictor-corrector method [1]. The idea of including both the manifold and connection conditions in the continuation equations has already been used in the literature. See [42], for maps, and [10, 13, 15, 29], for flows. In the last two references, all the conditions are stated in terms of boundary value problems in order to use the continuation package AUTO [16].

In our approach, the continuation equations are stated in terms of matching conditions on Poincaré sections. The system of equations and its differential with respect to the unknowns is evaluated by direct numerical integration of the differential equations, together with its first and second variational equations. The instability due to the hyperbolic character of all the p.o. considered is avoided by using multiple shooting (see Sect. 2.2).

Our attention has been restricted to homoclinic connections of periodic orbits, but the method generalizes naturally to heteroclinic connections of p.o., and also to homoclinic and heteroclinic connections of invariant tori. In this latter case, since the computation of d -dimensional tori for $d \geq 2$ is demanding in terms of computing time, it is necessary to pre-compute

and store the families of tori before attempting the numerical continuation of connections. This is currently work in progress (see [35] for preliminary results). Also, the numerical methodology has been applied to the RTBP only, but the continuation method make no use of any particularity of the RTBP other than its Hamiltonian character, and is thus valid for any other Hamiltonian system.

In Sect. 2, we briefly recall the RTBP and describe the numerical method used for the continuation of families of homoclinic connections of periodic orbits.

Sect. 3 is devoted to numerical results. In Sect. 3.1, we consider the equilibrium points L_1 and L_2 . For the LPO around L_1 , we have fixed the mass parameter μ to the Earth-Moon case, $\mu = \mu_{EM} = 9.53875 \cdot 10^{-4}$, in order to test the results obtained by our methodology with previous papers. We have continued, in a systematic way, the families of homoclinic orbits surrounding the Earth and those surrounding the Moon. In this latter case, a particular contribution of this paper is that besides recovering some of the families computed in [7, 8], we have been able to continue them for larger values of the energy. For such higher energy levels, connections can be found with close passages to Earth and Moon, which make them interesting as trajectories for the transportation of cargo in the Earth–Moon system (see Fig. 4 top right and [9]). With respect to the LPO around L_2 we have also fixed $\mu = \mu_{EM}$ and we have done a systematic continuation of families of homoclinic connections surrounding only the Moon, and those surrounding both the Earth and the Moon. We remark that, taking other values of μ , the same methodology allows to recover the homoclinic orbits obtained in [32, 40, 41].

The L_3 case has been much less investigated. From an astronomical point of view, horseshoe motion, explaining the motion of the co-orbital satellites, Janus and Epimetheus, of Saturn (see [31]) and near Earth asteroids (see [12]), has drawn some attention. In [4], it is seen that the manifolds of both L_3 and its corresponding LPO family play a role in horseshoe motion. Furthermore, there is numerical evidence [18, 20, 38] on the fact that the stable/unstable manifolds of the objects (LPO and 2D tori) of the center manifold of L_3 in the 3D RTBP confine regions of effective stability around the triangular points L_4 and L_5 . The extension of the methodology of this paper to the computation of connections of tori mentioned above would provide a new numerical tool for the analysis of the normal behavior of the center manifold of L_3 .

Sect. 3.2 is devoted to the computation of homoclinics of LPO around L_3 in the 2D RTBP, where some families of either half-horseshoe and full-

horseshoe shaped homoclinic orbits are computed. A systematic exploration is done for the Sun–Jupiter mass parameter. Some comments are made on the difficulty of the visualization of sections of the manifold tubes, due to the slow dynamics around L_3 , that produces intricate loops on the manifold tubes when the base LPO is large.

All the families of homoclinics computed correspond to first order homoclinic orbits, in the sense that they correspond to the first cuts of the manifold tubes. It is well known that, once a stable manifold tube intersects transversally an unstable one, giving rise to some homoclinics, an infinity of additional homoclinics exist associated with subsequent cuts of these same manifold tubes. We do not compute any of this “higher order” homoclinics, although we make some comments on its existence for the L_3 case in Sect. 3.2.3. In this Section we also illustrate, on a specific example, the classification of trajectories in transit and non–transit orbits as defined by Conley [11], and explore the possibility of obtaining trajectories with prescribed itineraries.

2 Homoclinic connections of Lyapunov p.o. of the RTBP

2.1 The RTBP

The circular restricted three–body problem (RTBP) describes the motion of a particle of infinitesimal mass, moving under the gravitational influence of two massive bodies called primaries, that describe circular orbits around their common center of mass. We will consider the planar problem, in which the motion of the third body is contained in the plane of motion of the primaries. Taking a coordinate system reference that rotates with the primaries, with origin placed at their center of mass, and suitable units, we can assume that the primaries have masses $1 - \mu$ and μ , $\mu \in (0, 1/2]$, their positions are fixed at $(\mu, 0)$ and $(\mu - 1, 0)$ and the period of their motions is 2π . With these assumptions, the equations of motion of the third body in this rotating (also called synodical) system of coordinates, are (see Szebehely [39])

$$\begin{aligned} \ddot{x} - 2\dot{y} &= D_x\Omega(x, y), \\ \ddot{y} + 2\dot{x} &= D_y\Omega(x, y), \end{aligned} \tag{1}$$

where

$$\Omega(x, y) = \frac{1}{2}(x^2 + y^2) + \frac{1 - \mu}{r_1} + \frac{\mu}{r_2} + \frac{1}{2}\mu(1 - \mu),$$

$r_1 = \sqrt{(x - \mu)^2 + y^2}$ and $r_2 = \sqrt{(x - \mu + 1)^2 + y^2}$. The system of equations (1) has a first integral, called the Jacobi integral, which is given by

$$C = 2\Omega(x, y) - \dot{x}^2 - \dot{y}^2. \quad (2)$$

Furthermore, we recall that equations (1) satisfy the well known symmetry

$$(t, x, y, \dot{x}, \dot{y}) \longrightarrow (-t, x, -y, -\dot{x}, \dot{y}). \quad (3)$$

This implies that, for each solution of equations (1), there also exists another one, which is seen as symmetric with respect to $y = 0$ in configuration space.

By introducing momenta $p_x = \dot{x} - y$ and $p_y = \dot{y} + x$, the equations of motion of the RTBP transform into the following Hamiltonian system

$$\begin{aligned} \dot{x} &= p_x + y, & \dot{p}_x &= p_y - \frac{(1 - \mu)(x - \mu)}{r_1^3} - \frac{\mu(x - \mu + 1)}{r_2^3}, \\ \dot{y} &= p_y - x, & \dot{p}_y &= -p_x - y \left(\frac{1 - \mu}{r_1^3} + \frac{\mu}{r_2^3} \right), \end{aligned} \quad (4)$$

with associated Hamiltonian function

$$H(x, y, p_x, p_y) = \frac{1}{2}(p_x^2 + p_y^2) - xp_y + yp_x - \frac{1 - \mu}{r_1} - \frac{\mu}{r_2}.$$

Its relation with the Jacobi integral is given by

$$C = -2H + \mu(1 - \mu).$$

The value of the Hamiltonian on each orbit will be referred as the *energy* of the orbit from now on.

We also recall that the RTBP has five equilibrium points: the collinear points, L_1 , L_2 and L_3 , situated on the line containing the primaries, and the equilateral ones, L_4 and L_5 , both forming an equilateral triangle with the two primaries. We denote by C_i and h_i the value of the Jacobi constant and the energy at the equilibrium point L_i , $i = 1, \dots, 5$.

We focus our attention on the dynamics of the RTBP around the collinear equilibrium points L_1 , L_2 and L_3 . The position and the energy of the collinear points is given in terms of μ in Table 1 (see [39]). Observe that $x_{L_2} \leq \mu - 1 \leq x_{L_1} \leq \mu \leq x_{L_3}$, that is, L_1 is between both primaries, L_2 is on the left hand side of the small one and L_3 is on the right hand side of the large one.

It is well known that, if we write the differential equations (4) as

$$\dot{x} = X_H(x)$$

Table 1: Position on the synodical horizontal axis and energy of the collinear equilibrium points

	x_{L_i}	h_i
L_1	$-1 + \left(\frac{\mu}{3}\right)^{1/3} - \frac{1}{3} \left(\frac{\mu}{3}\right)^{2/3} + \frac{26}{9} \left(\frac{\mu}{3}\right) + O(\mu^{4/3})$	$-\frac{3}{2} - \frac{9}{2} \left(\frac{\mu}{3}\right)^{2/3} + 5 \left(\frac{\mu}{3}\right) + O(\mu^{4/3})$
L_2	$-1 - \left(\frac{\mu}{3}\right)^{1/3} - \frac{1}{3} \left(\frac{\mu}{3}\right)^{2/3} + \frac{28}{9} \left(\frac{\mu}{3}\right) + O(\mu^{4/3})$	$-\frac{3}{2} - \frac{9}{2} \left(\frac{\mu}{3}\right)^{2/3} + 7 \left(\frac{\mu}{3}\right) + O(\mu^{4/3})$
L_3	$1 + \frac{5}{12} \mu + O(\mu^3)$	$-\frac{3}{2} - \frac{1}{2} \mu + O(\mu^2)$

then $\text{Spec } DX_H(L_i) = \{\pm i\omega, \pm\lambda\}$, so the equilibrium point L_i , $i = 1, 2, 3$ is a center \times saddle point and Lyapunov's center theorem (see, for example, [33]) applies. Thus, the equilibrium point gives rise to a one-parametric family of periodic orbits, spanning a 2-D manifold tangent to real and imaginary parts of the eigenvectors of eigenvalues $\pm i\omega$ at the equilibrium point. This family is known as Lyapunov family of periodic orbits (LPO), and, close to the equilibrium point, it can be parameterized by the energy H .

Since the equilibrium point is hyperbolic, the Lyapunov family inherits hyperbolicity and therefore the periodic orbits have, at least close to the equilibrium point, unstable and stable manifolds. These unstable and stable manifolds can intersect, giving rise to homoclinic connections of the LPO.

2.2 Numerical methodology

An homoclinic connection of an object X is a trajectory that tends forward and backward in time to X . Thus, it lies in the intersection of the unstable and stable manifolds of the object $W^u(X) \cap W^s(X)$. An heteroclinic connection between two objects X, Y is a trajectory that tends backward in time to X and forward in time to Y , so it lies in $W^u(X) \cap W^s(Y)$. Although in the present paper we will restrict ourselves to the computation of homoclinic connections, all the methodology applies with minor modifications to the computation of heteroclinic connections.

Consider a periodic orbit (p.o.) X with hyperbolic character, and assume that we have a parametrization of its unstable and stable manifold tubes that can be numerically evaluated. We denote these parameterizations as $\psi^u(\theta, \xi)$ and $\psi^s(\theta, \xi)$, where θ is an angle and $\xi \in \mathbb{R}$ (we give actual formulae later on this Section). We also assume that $\psi^{u/s}(\theta, \xi)$ describes the periodic orbit for $\xi = 0$, one branch of the manifold for $\xi > 0$, and the other branch for $\xi < 0$. We will denote these branches as $W_+^{s/u}(X)$ and $W_-^{s/u}(X)$, respectively.

Let $\Sigma = \{g(x) = 0\}$ be a hypersurface which is known to be intersected by the manifold tubes, where $g : \mathbb{R}^4 \rightarrow \mathbb{R}$ is a function defined on a neigh-

borhood of this intersection. Given a point x , we consider two associated Poincaré maps: P_Σ^+ , which propagates the flow forward in time until the next intersection with Σ , and P_Σ^- , which does the same backward in time. Choose a value ξ_0 , with $|\xi_0|$ small, and consider the function

$$F(\theta^u, \theta^s) = P_\Sigma^+(\psi^u(\theta^u, \xi_0)) - P_\Sigma^-(\psi^s(\theta^s, \xi_0)) \quad (5)$$

The values of (θ^u, θ^s) for which $F(\theta^u, \theta^s)$ is zero correspond to a homoclinic connection. In particular, the points $\psi^u(\theta^u, \xi_0)$, which is close to the p.o. in $W^u(X)$, $\psi^s(\theta^s, \xi_0)$, also close to the p.o. in $W^s(X)$, and $P_+(\psi^u(\theta^u, \xi_0)) = P_-(\psi^s(\theta^s, \xi_0))$, which is in Σ , belong to the homoclinic connection.

The function F and its differential DF can be numerically evaluated by numerical integration of $\dot{x} = X_H(x)$ and its first variational equations, so Newton's method can be used to find roots of F . In order to obtain initial conditions for the Newton iteration, it is convenient to display the intersection of each manifold tube with the section Σ , $\{P_\Sigma^+(\psi^u(\theta, \xi_0))\}_{\theta \in [0, 2\pi]}$ and $\{P_\Sigma^-(\psi^s(\theta, \xi_0))\}_{\theta \in [0, 2\pi]}$. Since the manifolds are 2D tubes, each intersection is a 1-dimensional set (typically closed curves) as, for instance, in Figure 2. Each common point of these two sets gives rise to a homoclinic connection, and therefore corresponds to a zero of F .

The section Σ that defines the P_Σ^+ and P_Σ^- Poincaré maps should be defined locally, in a neighborhood of the intersection of the manifold tubes. In practice, it is more convenient to work with global sections defined by an implicit equation $\{g(x) = 0\}$ (actually, in all the computations of Sect. 3 we have used just hyperplanes). It may happen then that the first cut with the section is not the one we are interested in. For instance, in Figure 1, in order to match in $\Sigma = \{x = 0\}$ the first cut of the unstable manifold with the stable manifold, we need to consider the sixth cut of the stable manifold with Σ . In what follows, we will denote the j -th cut of a branch of manifold with a section Σ by $W_\pm^{s/u}(X) \cap \Sigma^j$.

In order to develop actual formulae for the invariant manifold tubes of the p.o., assume that x_0 is an initial condition of a T -periodic orbit (p.o.), so that $\phi_T(x_0) = x_0$. The p.o. can be parameterized by an angle as

$$\varphi(\theta) = \phi_{\frac{\theta}{2\pi}T}(x_0).$$

Assume that $\Lambda > 0$ is an eigenvalue of the monodromy matrix¹ $D\phi_T(x_0)$ ($\Lambda > 1$ for the unstable manifold, $\Lambda < 1$ for the stable one), and $v_0 \in \mathbb{R}^4$ is

¹For $\Lambda < 0$, a real Floquet change is not possible. In such a case, we can consider the p.o. $2T$ -periodic and work with $D\phi_T(x_0)^2 = D\phi_{2T}(x_0)$, which will have $\Lambda^2 > 0$ as corresponding eigenvalue. This has never happened in the computations of Sect. 3.

a corresponding eigenvector. We define

$$v(\theta) = \Lambda^{-\theta/2\pi} D\phi_{\frac{\theta}{2\pi}T}(x_0)v_0, \quad (6)$$

which is the eigenvector associated to the point $\varphi(\theta)$, and

$$\bar{\psi}(\theta, \xi) = \varphi(\theta) + \xi v(\theta).$$

Then $\bar{\psi}(\theta, \xi)$ gives the linear approximation of the invariant manifold $\psi(\theta, \xi)$, for $|\xi|$ small enough, that is, close to the periodic orbit. In order to find homoclinic connections, we will use $\bar{\psi}$. Furthermore, a first-order Taylor expansion shows that, for bounded $|t|$,

$$\phi_t(\bar{\psi}(\theta, \xi)) = \bar{\psi}(\theta + t\omega, e^{t\lambda}\xi) + O(\xi^2) \quad (7)$$

for $\omega = 2\pi/T$, $\lambda = \omega \ln \Lambda / (2\pi)$. Therefore, the manifold parameterized by $\bar{\psi}(\theta, \xi)$ is invariant by the flow except for a quadratic term in ξ . In all the computations done along the paper we have taken $|\xi|$ of the order of 10^{-6} .

For the continuation of homoclinic connections, we will consider the energy H as a parameter. This means that, for each value of the energy we need to compute the corresponding p.o., its eigenvalues and eigenvectors, and a new initial seed in order to solve the equations $\{F(\theta^u, \theta^s) = 0\}$ with F defined as in (5). We would like to automatize the procedure in a standard predictor-corrector method (see [1]). This implies to consider the eigenvalues and eigenvectors as functions of the initial conditions of the p.o. This is not convenient in order to do continuation, because, although they can be obtained by a general eigenvalue routine (such as LAPACK's DGEEV, [2]), it is not obvious how to differentiate them with respect to the initial conditions of the p.o. An strategy is to add the eigenvalue condition to the continuation equations, plus a normalization condition in order to have local uniqueness of the eigenvectors. See also a similar approach in [5, 15, 28, 29].

Consider the following variables. Let $h \in \mathbb{R}$ be an energy level, $x \in \mathbb{R}^4$ an initial condition of a p.o. of period T , $\Lambda^u, \Lambda^s \in \text{Spec } D\phi_T(x)$, with $\Lambda^u > 1$ and $0 < \Lambda^s < 1$, and v^u, v^s corresponding eigenvectors of $D\phi_T(x)$. Let us also consider $\theta^u, \theta^s \in [0, 2\pi]$ starting phases on the linear approximation of the unstable and stable manifolds, respectively. We introduce $T^u, T^s \in \mathbb{R}$ the times to intersect the section Σ from the starting points $\bar{\psi}^u(\theta^u, \xi), \bar{\psi}^s(\theta^s, \xi)$ on the (linear approximation of the) unstable and stable manifolds, respectively (for a given ξ). Notice that the introduction of T^u, T^s avoids the need to take into account the number of cuts of the sections, which would have been necessary if we had considered Poincaré maps explicitly, as in the function F defined in (5).

We also consider $g_1 : \mathbb{R}^4 \rightarrow \mathbb{R}$ a function defining a Poincaré section for the periodic orbit, and $g_2 : \mathbb{R}^4 \rightarrow \mathbb{R}$ a function defining the Poincaré section to match the manifolds, this is, $\Sigma = \{g_2(x) = 0\}$. The system of equations we consider in order to continue homoclinic connections of p.o. is

$$\begin{aligned}
 H(x) - h &= 0, \\
 g_1(x) &= 0, \\
 \phi_T(x) - x &= 0, \\
 \|v^u\|^2 - 1 &= 0, \\
 D\phi_T(x)v^u - \Lambda^u v^u &= 0, \\
 \|v^s\|^2 - 1 &= 0, \\
 D\phi_T(x)v^s - \Lambda^s v^s &= 0, \\
 g_2\left(\phi_{T^u}(\bar{\psi}^u(\theta^u, \xi_0))\right) &= 0, \\
 g_2\left(\phi_{T^s}(\bar{\psi}^s(\theta^s, \xi_0))\right) &= 0, \\
 \phi_{T^u}(\bar{\psi}^u(\theta^u, \xi_0)) - \phi_{T^s}(\bar{\psi}^s(\theta^s, \xi_0)) &= 0,
 \end{aligned} \tag{8}$$

where ξ_0 is kept fixed to a small value (usually 10^{-6}), and the unknowns are

$$h, x, T, \Lambda^u, v^u, \Lambda^s, v^s, \theta^u, T^u, \theta^s, T^s.$$

Here $T, T^u > 0$ and $T^s < 0$.

In our setting, the integration times T^u, T^s may become large (this is the case in Sect. 3.2). In order to maintain high precision, it is necessary to use multiple shooting. We have implemented a system with multiple shooting both in the periodic orbit and the connection.

Either with the simple or multiple shooting equations, continuation has been done by a standard predictor–corrector method [1]. In order to differentiate any of the systems of equations used, it is needed to integrate the second variational equations of the RTBP. Note also that, both in the single and multiple shooting cases, the system is over–determined and rank deficient. For instance, a clear over–determination is the fact that, the two last equations of Eq. (8) imply the third equation from the bottom. The reason for that redundancy follows from numerical experience, and its goal is to accelerate the convergence of Newton’s method. Redundancy and rank–deficiency can be coped by using the minimum–norm least–squares (LS) solution for the linear system that gives the Newton correction. Of course, we could also eliminate redundant equations, but this would need a linear analysis that would lead to an avoidable computational overhead. The computation of the minimum–norm LS does implicitly this linear analysis at negligible computational cost. In our implementation, this solution has

been computed using QR decomposition with column pivoting. For more details, see [24, 34].

Of course, the system of equations in Eq. (8) is not specific of the RTBP but is valid for any Hamiltonian system. With minor modifications, it would allow to continue heteroclinic connections of p.o., as it has been mentioned in the Introduction.

3 Numerical results

The remaining part of the paper is devoted to present our results. First, in Sect. 3.1 we consider the case of L_1 and L_2 for the Earth-Moon value of the mass parameter $\mu = \mu_{EM} = 1.215058560962404 \times 10^{-2}$. As mentioned in the introduction, we compute some families of homoclinic connections to planar Lyapunov orbits that surround the small primary (the Moon), in order to compare the results obtained with the numerical techniques presented in this paper with the results obtained by Canalias and Masdemont in [8] using Lindstedt-Poincaré series. Furthermore, we compute families of homoclinic connections of Lyapunov orbits that surround either only the large primary (the Earth) or both primaries. We remark that in [30] the authors give asymptotic expressions of the invariant manifolds of Lyapunov orbits around L_1 that, for small values of μ and energies close to the one of L_1 , allow them to prove the existence of homoclinic connections analogous to the ones computed here.

After that, in Sect. 3.2 we explore the neighborhood of L_3 point for the Sun-Jupiter mass parameter $\mu = \mu_{SJ} = 9.53875 \times 10^{-4}$. Additional comments are made on the geometry of manifold tubes and the possibility to apply symbolic dynamics.

It is known that the existence of an homoclinic connection implies the existence of an infinite number of homoclinics. For maps, this is a consequence of Birkhoff's homoclinic theorem [6] (see also [36]). In all the explorations that follow, we have computed only homoclinics corresponding to the first cuts of the manifold tubes. We refer to these homoclinics as "first-order homoclinics". The existence of higher-order homoclinics is illustrated in Sect. 3.2.3.

All the homoclinic orbits have been computed with tolerances ranging from 10^{-10} to 10^{-12} , that is, the non-linear systems of equations of the previous Section used for continuation are satisfied within this accuracy. The continuations are stopped when the accuracy criterion is violated. In general, this happens when a passage close to the small primary takes place.

In some figures where the projection of orbits or invariant manifolds in configuration space is shown, we have included the horizontal line $y = 0$ (dotted line in the plots) that contain the primaries for greater clarity. Blue and red indicate that the piece of orbit or the set of points shown belongs to the stable and unstable manifold respectively. As it has been mentioned at the end of the introduction, we will only compute first-order homoclinics, although some comments will be made on the existence of higher-order homoclinics for the L_3 case in Sect. 3.2.3.

3.1 Homoclinic connections to Lyapunov orbits around L_1 and L_2

In this Section we have fixed the value of the mass parameter to $\mu = \mu_{EM}$. As it has been mentioned before, L_1 and L_2 are center×saddle equilibrium points, and for values of the energy close to h_1 and h_2 (given in Table 1) respectively, the planar Lyapunov periodic orbits (LPO) around them inherit their hyperbolic behavior, so they have stable and unstable invariant manifolds.

Let X be a hyperbolic invariant object, and $W^{u/s}(X)$ the unstable/stable manifold (or simply $W^{u/s}$ when no confusion is possible). In the case of the collinear equilibrium points, $X = L_i$, $i = 1, 2$, both the stable and unstable manifolds have a branch to the right and a branch to the left of L_i (see [11] for a proof). In the present Section, we denote by $W_+^{u/s}(L_i)$, $i = 1, 2$, the branch corresponding to the eigenvector that points to the right half space $\{x > x_{L_i}\}$, and by $W_-^{u/s}(L_i)$, $i = 1, 2$, the branch corresponding to the eigenvector pointing to the left half region $\{x < x_{L_i}\}$. This will be coherent with the notation for the branches introduced above as long as we take v_0 in Eq. (6) with positive x component. We extend this notation for the branches of the invariant manifolds of a periodic orbit, which are two dimensional objects than can be viewed as tubes approaching the LPO. In Fig. 1 and 5 some of these invariant manifolds are plotted. Due to the symmetry (3), and the fact that LPO are symmetric with respect the $y = 0$ axis, the branches W_-^u and W_-^s are symmetric, as well as W_+^u and W_+^s are. By numerically propagating the manifolds, it is seen that, in order to find connections, it only makes sense to try to match branches in the same half space (see Fig. 1 and 5).

Recall that we denote the j -th cut of the W_{\pm}^u manifold tube forward in time by $W_{\pm}^u \cap \Sigma^j$, and the k -th cut of the W_{\pm}^s manifold tube backward in time by $W_{\pm}^s \cap \Sigma^k$. We will say that there exists a homoclinic connection of

type $(-j, -k)$ or $(+j, +k)$, $j, k \in \mathbb{N}$, if

$$(W_-^u \cap \Sigma^j) \cap (W_-^s \cap \Sigma^k) \neq \emptyset, \quad \text{or} \quad (W_+^u \cap \Sigma^j) \cap (W_+^s \cap \Sigma^k) \neq \emptyset, \quad (9)$$

respectively. We observe that, in both cases, all the pairs k', j' such that $k' + j' = k + j$ give the same homoclinic connection. Depending on the equilibrium point and the branches we consider, we will obtain homoclinic orbits that surround either only one primary or both primaries.

For L_1 and L_2 , we will work with Poincaré sections of the form $\Sigma = \{x = \text{constant}\}$. Given an LPO of energy level h , all its homoclinics will lie in the manifold $\{H = h\}$, which is three-dimensional. In this manifold, Σ is a plane that can be visualized by projecting in the (y, p_y) (or (p_x, p_y)) coordinates. The projections of the sets defined in (9) are used to find initial homoclinic connections. These initial connections are then continued by the method described above giving rise to families.

Each family can be represented by a characteristic curve, that will be displayed in the (h, y_f) plane, where h is the energy and y_f the value of the y coordinate of the corresponding point in the set defined by Eq. (9). During the continuation of a family, we have also plotted the sets of Eq. (9) for several energy levels, in order to check for the appearance of new families of connections, as in Fig. 6.

3.1.1 Homoclinics to LPO of L_1

When we consider the branches of each invariant manifold, we see that W_-^u, W_-^s surround the small primary, while W_+^u, W_+^s surround the large one (see Fig. 1). So we will look for families of homoclinic orbits that surround only one primary (the Earth or the Moon).

For the homoclinics surrounding the Earth, we use $\Sigma = \{x = 0\}$. Considering the first cut of W_+^u with Σ , it is seen in Fig. 1 that, in order to find a connection, we need to consider the sixth cut of W_-^u with Σ . Therefore, first-order homoclinics are given by the intersection of $W_+^u \cap \Sigma^1$ with $W_+^s \cap \Sigma^6$, whose representation in the (y, p_y) plane for a specific value of the energy is the left plot in Fig. 2. We can observe four points of intersection, so we can follow four different families of homoclinic orbits that surround the Earth. We denote them by He_j , $j = 1, 2, 3, 4$. The orbits in the families $\text{He}_{3,4}$ are symmetric (with respect the horizontal axis), while the orbits in the families $\text{He}_{1,2}$ are not (one family is obtained from the other by applying symmetry (3)). The characteristic curves of all of these families are shown in Fig. 3 left. The computations of the families are done using the section

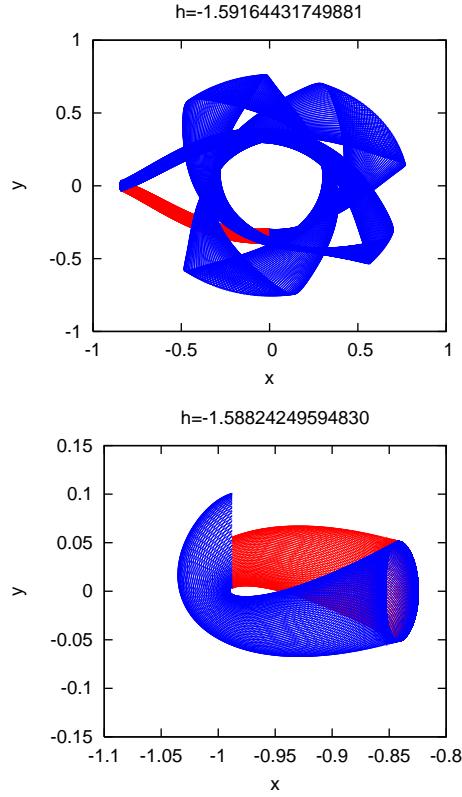


Figure 1: Invariant manifolds associated with a Lyapunov orbit around L_1 , for the Earth-Moon mass parameter and the energies indicated. Left: branches W_+^u, W_+^s up to their first and sixth intersection, respectively, with $\Sigma = \{x = 0\}$. Right: branches W_-^u, W_-^s up to their first and second intersection, respectively, with $\Sigma = \{x = \mu - 1\}$.

$\{x = -1/2\}$. In Fig. 4, first row, several homoclinics surrounding the Earth from different families are shown.

For the homoclinics surrounding the Moon, we fix $\Sigma = \{x = \mu - 1\}$. Proceeding as above (see Fig. 1 right), we conclude that first-order homoclinics are given by the intersection of the sets $W_+^u \cap \Sigma^1$ and $W_+^s \cap \Sigma^2$ (see Fig. 2 right). Only two homoclinic orbits are found for the levels of energy explored. The characteristic curves of all of these families are shown in Fig. 3 right, denoted by Hm_j , $j = 1, 2$. Observe that the family Hm_2 is such that y_f approaches the zero value. This means that the family tends to a collision orbit with the Moon. In order to follow the family for higher values of the

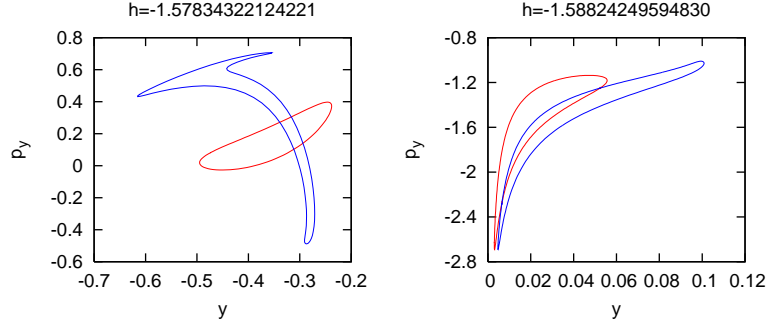


Figure 2: Left: Sets $W_+^u \cap \Sigma^1$ and $W_+^s \cap \Sigma^6$ in the (y, p_y) plane for a Lyapunov orbit around L_1 at the section $\Sigma = \{x = 0\}$. Right: Sets $W_-^u \cap \Sigma^1$ and $W_-^s \cap \Sigma^2$ in the (y, p_y) plane for a Lyapunov orbit around L_1 at the section $\Sigma = \{x = \mu - 1\}$. Both plots correspond to $\mu = \mu_{EM}$.

energy, a regularization of the equations should be done. Furthermore, it can be seen that the numerical procedure of Sect. 2.2 allows to reach energy levels on which LPO are large. In Fig. 4, second row, several homoclinics surrounding the Moon from different families are shown.

Associated to any of these families, there are families of higher-order homoclinics that perform more revolutions around the corresponding body. In [8], homoclinic connections that perform several revolutions around the Moon can be found.

3.1.2 Homoclinics to LPO of L_2

When we consider the branches of each invariant manifold of the LPO family around L_2 , we see that W_+^u, W_+^s surround the small primary, while W_-^u, W_-^s surround both primaries (see Fig. 5). So we will look for families of homoclinic orbits that surround either only the Moon or both the Earth and the Moon.

For the homoclinics surrounding both the Earth and the Moon, we consider the section $\Sigma = \{x = 0\}$. From Fig. 5 left, it is seen that first order homoclinics are given by the intersection of $W_-^u \cap \Sigma^1$ with $W_-^s \cap \Sigma^2$. In Fig. 6, the curves $W_-^u \cap \Sigma^1$, $W_-^s \cap \Sigma^2$ are represented in the (p_x, p_y) plane for different energy values. Clearly, as the energy increases, new families of first-order homoclinic connections appear. We denote them as Ho_j , $j = 1, 2, \dots$. We compute up to 12 different families, whose characteristic curves are plotted in Fig. 8 left. It can be seen that the orbits of the families labelled as

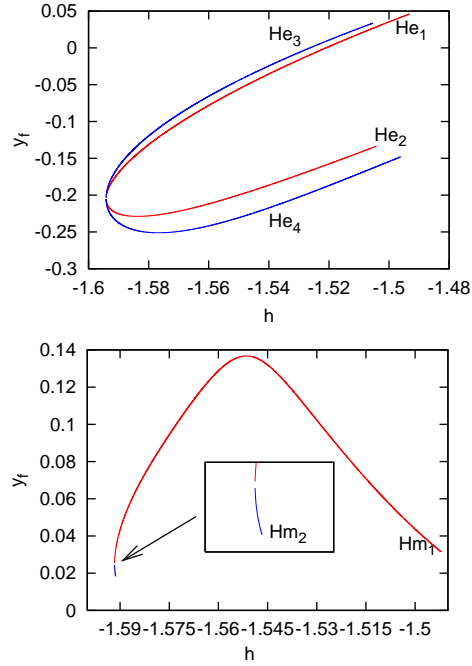


Figure 3: Left: characteristic curves of families of homoclinic orbits that surround the Earth (the points on the curves correspond to $\Sigma = \{x = -0.5\}$). Right: characteristic curves of families of homoclinics surrounding the Moon (the points on the curves correspond to $\Sigma = \{x = \mu - 1\}$). Both curves are given in the (h, y_f) plane.

Ho_j , $j = 1, 2, 5, 6, 9, 10$ are symmetric orbits, while the orbits of the families Ho_j , $j = 3, 4, 7, 8, 11, 12$ are not. In Fig. 9, first row, several homoclinics to Lyapunov orbits around L_2 from different families Ho_j are shown.

For the homoclinics surrounding only the Moon, we consider the section $\Sigma = \{x = \mu - 1\}$. From Fig. 5 right, we conclude that first order homoclinics are given by the intersection of $W_+^u \cap \Sigma^1$ and $W_+^s \cap \Sigma^2$, which are represented in the (p_x, p_y) plane in Fig. 7 for two energy levels. We can observe two points of intersection, so we can follow two different families of homoclinic orbits that surround once the small primary, denoted by Hi_1 and Hi_2 . Their characteristic curves are plotted in Fig. 8 right. In Fig. 9, second row, several homoclinics to Lyapunov orbits around L_2 from different families Hi_1 are shown.

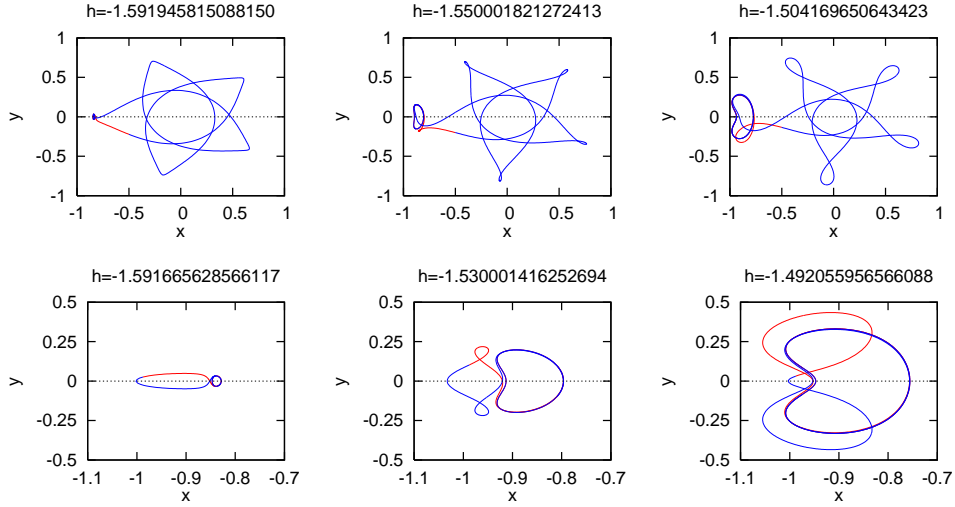


Figure 4: Projection in the configuration space of some homoclinic orbits to a LPO around L_1 . First row: orbits from the family He_1 . Second row: orbits from the family Hm_1 .

3.2 Homoclinic connections of Lyapunov orbits around L_3

One main difference between L_3 and $L_{1,2}$ is that, around this point, semi-analytical techniques give accurate representations in a very small energy range (see [26]). Therefore, they cannot be used for the computation of Lyapunov orbits and manifolds around L_3 as they have been used around the L_1 and L_2 points [8, 22, 23, 26]. In contrast with the previous section, the value of the mass parameter used has been chosen to be Sun–Jupiter mass ratio ($\mu_{SJ} = 0.000953875$), in order to relate our results to previous works on horseshoe motion [3, 4, 31].

The numerical computations of homoclinic orbits to LPO around L_3 presented in this Section are the first ones the authors are aware of. Because of this reason, in addition to the exploration of families of first-order homoclinics, some additional comments on the existence of infinitely many homoclinics and the geometry manifold tubes will be made in Sect. 3.2.3.

Due to the behavior of the manifolds of Lyapunov orbits around L_3 (see Fig. 10), we will change the notation for branches of manifolds with respect to the one of L_1 and L_2 . For a Lyapunov orbit X , $W_+^{u/s}(X)$ will denote the branch of the unstable or stable manifold in the $\{y > 0\}$ half-space, whereas $W_-^{u/s}(X)$ will refer to the branch in the $\{y < 0\}$ half-space. The branch

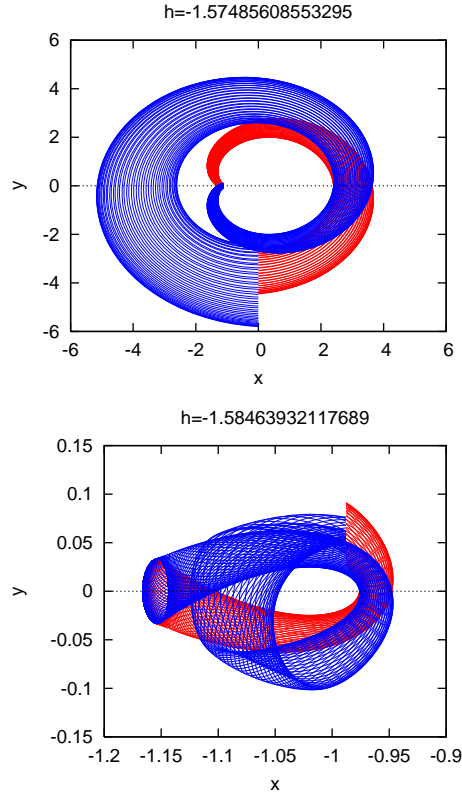


Figure 5: Invariant manifolds associated with a Lyapunov orbit around L_2 for the Earth-Moon mass parameter and the energies indicated. Left: branches $W_-^{u/s}$ up to their second and third intersection respectively with $\Sigma = \{x = 0\}$. Right: branches $W_+^{u/s}$ up to their second and third intersection respectively with $\Sigma = \{x = \mu - 1\}$.

$W_-^u(X)$ can be obtained from the branch $W_+^s(X)$ by applying the symmetry (3) and vice-versa, and the same happens for $W_-^s(X)$ and $W_+^u(X)$.

Another particularity of L_3 is that first-order homoclinics can be found by matching either branches of manifolds of the same half-space or branches of different half-spaces. The first type of connections have half-horseshoe shape, whereas the second one have full-horseshoe shape. They are explored in subsections 3.2.1 and 3.2.2, respectively. Since the times T^u, T^s of Eq. (8) are large (of the order of hundreds of RTBP dimensionless time units), multiple shooting is needed in order to have high precision. Typically we have

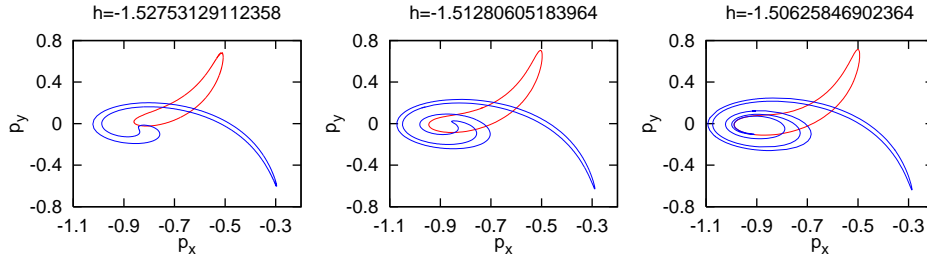


Figure 6: Curves $W_-^u \cap \Sigma^1$ and $W_-^s \cap \Sigma^2$ in the (p_x, p_y) plane for a Lyapunov orbit around L_2 for the Earth-Moon mass parameter and energies indicated.

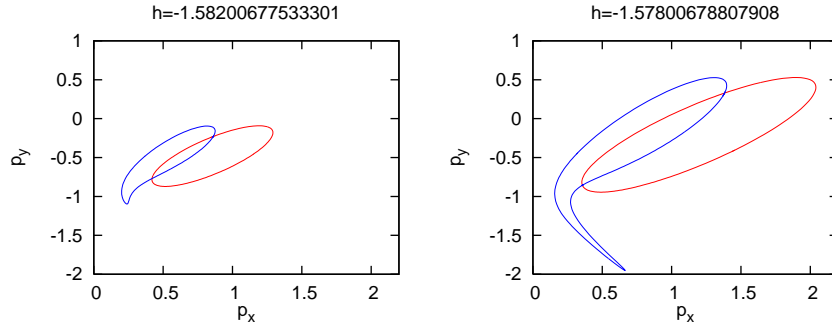


Figure 7: Intersections $W_+^u \cap \Sigma^1$ and $W_+^s \cap \Sigma^2$ in the (p_x, p_y) plane for a Lyapunov orbit around L_2 for the Earth-Moon mass parameter and the energies indicated. Both plots correspond to the section $\Sigma = \{x = \mu - 1\}$.

used from 6 to 10 intermediate points, suitably distributed, along the two pieces of the homoclinic orbit (on the unstable and stable manifolds), and a tolerance of 10^{-10} . When more than 10 intermediate points for the multiple shooting method are necessary to reach the desired precision, we have stopped the computations.

3.2.1 Homoclinics of branches of the same half-space

Due to the symmetry (3), for each homoclinic to a LPO corresponding to branches in $\{y < 0\}$, there is a symmetric one corresponding to branches in $\{y > 0\}$. Our exploration will be therefore limited to branches in $\{y < 0\}$. Using the section $\Sigma = \{x = \mu - 1/2\}$, it is found that first-order homoclinics in $\{y < 0\}$ are of type $(-1, -2)$, that is, they result from the intersection between the curves $W_-^u \cap \Sigma^1$ and $W_-^s \cap \Sigma^2$. Since the L_3 point does not

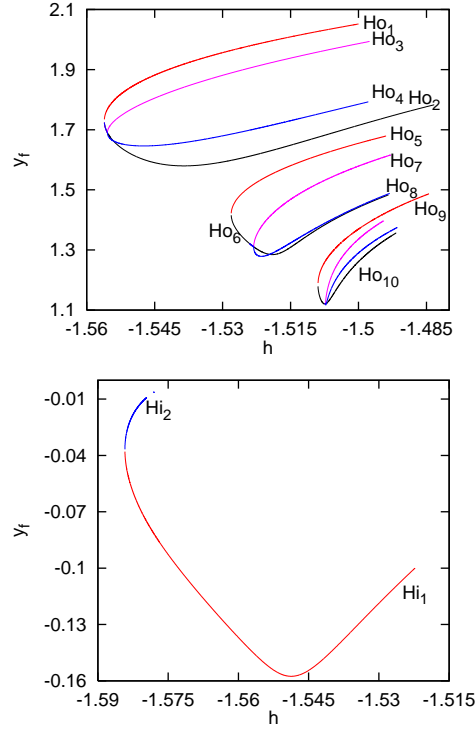


Figure 8: Characteristic curves in the (h, y_f) plane of families of homoclinic orbits that surround once either both primaries (left) or only the Moon (right).

have a homoclinic connection of this type, these curves do not intersect for values of the energy close to the value of the energy at L_3 , which is $h_3 = -1.500476927936$ (see Fig. 11, left). When increasing the energy, they become tangent at energy $h = h_t \simeq -1.5004766$, and, after that, they intersect transversally in two points (see Fig. 11, right). Therefore, we have two families of homoclinics, Hn_1 and Hn_2 , that we have followed by the continuation method in Sect. 2.2. Their characteristic curves are represented in Fig. 13 left.

Let us describe these homoclinic orbits in more detail. As it is shown in Fig. 10, the invariant manifolds present a half horseshoe shape until the first intersections with Σ . Orbits in these invariant manifolds have loops close to the LPO, that “straighten out” as they get away of it (see Fig. 12 left). The presence of loops in in horseshoe periodic orbits was analyzed from the $\mu = 0$ case in [4]. As energy increases, the manifolds become thicker and

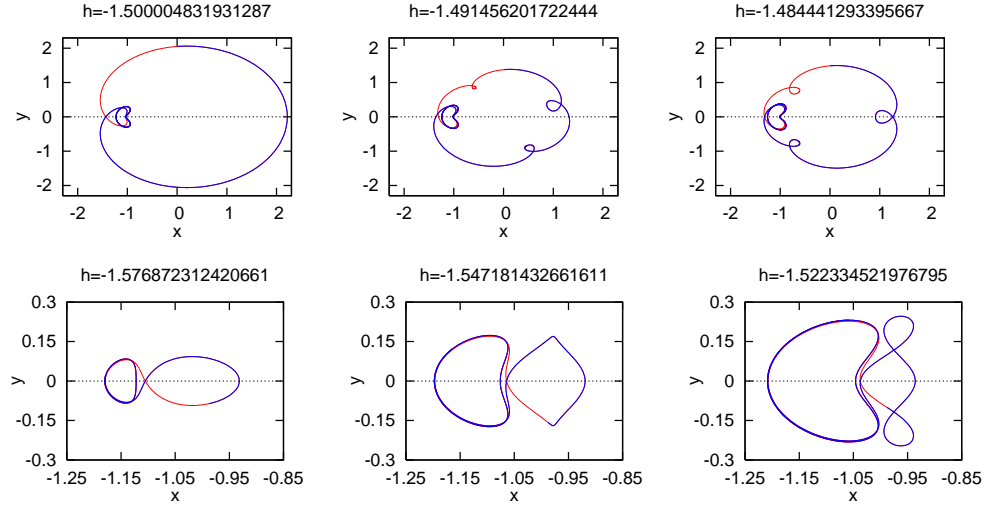


Figure 9: Projection in the configuration space of some homoclinic orbits to a LPO around L_2 . First row: orbits from families Ho_1 , Ho_{12} and Ho_9 . Second row: orbits from the family Hi_1 .

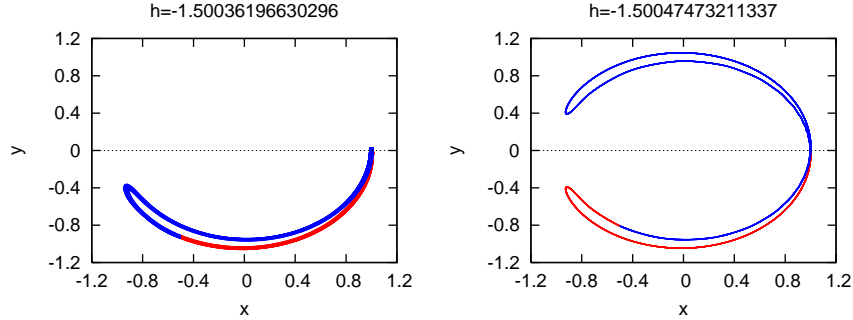


Figure 10: For $\mu = \mu_{SJ}$, projection in the configuration space of some orbits of different branches of the invariant manifolds (W^u in red, W^s in blue) associated with the Lyapunov orbits around L_3 for the energies indicated.

loops appear farther from the LPO, until they eventually reach the surface of section Σ . This happens at energy $h_l = -1.4994267$ (see Fig. 12 right). From this energy on, the representation of the sections of the manifold tubes with Σ is not straightforward, because, due to the presence of loops, different pieces of these sections are obtained by a different number of cuts with Σ (see Fig. 14). In this way, the $(\pm i, \pm j)$ classification of homoclinics stops

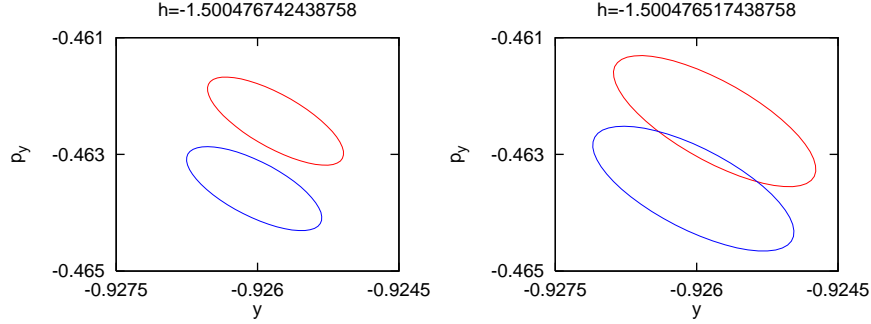


Figure 11: For $\mu = \mu_{SJ}$, (y, p_y) projections of $W_-^u \cap \Sigma^1$ (red) and $W_-^s \cap \Sigma^2$ (blue) curves at the section $\Sigma = \{x = \mu - 1/2\}$, for the values of the energies indicated.

making sense. This is not a problem for the continuation method of Sect. 2.2, because it does not make use of the number of cuts necessary in order to reach the section. But, in order to check for the appearance of new families of homoclinics, it is convenient to be able to have a clear representation of the section of the manifold tubes.

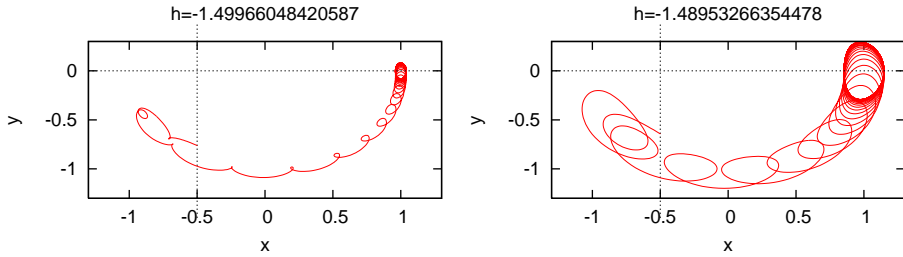


Figure 12: For $\mu = \mu_{SJ}$, projection in configuration space of some orbits of W_-^u up to their second intersection with Σ (plotted as a dotted line for clarity). As the energy increases, the loops reach a neighborhood of the section Σ .

This can be done if we can numerically evaluate a parametrization $\psi(\theta, \xi)$, with $\theta \in [0, 2\pi]$ and $\xi \in \mathbb{R}$ with $|\xi|$ not necessarily small. Assume that a section is given by $\Sigma = \{g(x) = 0\}$, for $g : \mathbb{R}^n \rightarrow \mathbb{R}$. Given starting values (θ_0, ξ_0) such that $\psi(\theta_0, \xi_0) \in \Sigma$, the curve intersection between the invariant manifold and Σ can be obtained by continuation of the equation

$$g(\psi(\theta, \xi)) = 0$$

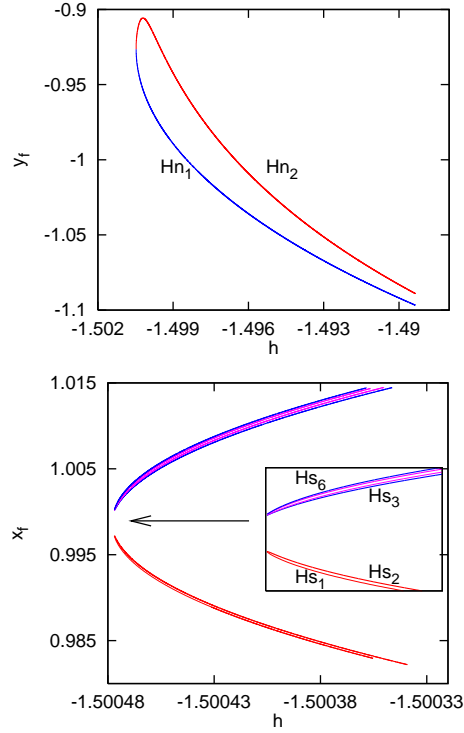


Figure 13: For $\mu = \mu_{SJ}$, characteristic curves of families of homoclinic orbits around LPO of L_3 . Left: families of type $(-1, -2)$ at the section $\Sigma = \{x = \mu - 1/2\}$ in the (h, y_f) plane. Right: families of symmetric homoclinic orbits of type $(-1, +1)$ at the section $\tilde{\Sigma} = \{y = 0\}$ in the (h, x_f) plane.

with respect to (θ, ξ) .

In order to numerically evaluate such a parametrization, assume there exists a function $\psi(\theta, \xi)$ parameterizing the manifold tube and satisfying $\phi_t(\psi(\theta, \xi)) = \psi(\theta + t\omega, e^{t\lambda}\xi)$, with ω, λ defined as in (7). Using this property, and switching ψ by its linear approximation $\bar{\psi}$ (introduced in Sect. 2.2) for small $|\xi|$, we can take

$$\psi(\theta, \xi) = \phi_{t^*} \left(\bar{\psi}(\theta - t^*\omega, e^{-t^*\lambda}\xi) \right),$$

for t^* such that $|e^{-t^*\lambda}\xi|$ is small.

The curves in Fig. 15 top have been obtained in this way. The initial values (θ_0, ξ_0) have been obtained starting from an arbitrary phase θ_* , $\xi_0 =$

10^{-6} , and computing the first cut with Σ of W_-^u and the second one of W_-^s . Special care has to be taken in order to check for the appearance of new families of homoclinics, since visual inspection can be misleading, as is illustrated in Fig. 15. For energy $h = -1.49602677$, a graph of the distance of each point of the curve $W_-^u \cap \Sigma^1$ to the curve $W_-^s \cap \Sigma^2$ (Fig. 15 bottom left) shows that in Fig. 15 top left there are only two intersections. The corresponding homoclinic connections are shown in Fig. 16. For energy $h = -1.489343$, the same kind of graph shows that in Fig. 15 top right there are 4 intersections, so two new families of homoclinics have appeared. We have not followed them.

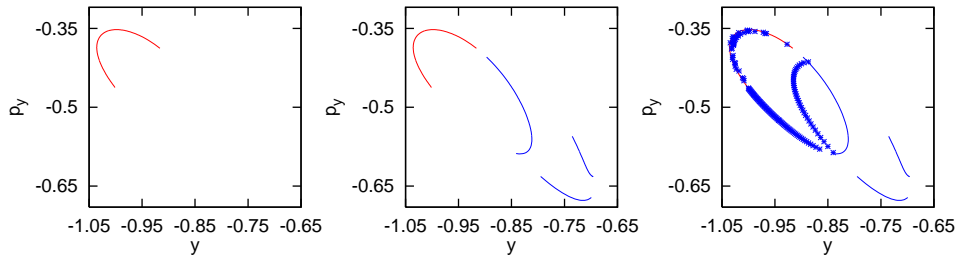


Figure 14: For $\mu = \mu_{SJ}$ and $h = -1.49602677$, (y, p_y) projection of curves $W_-^u \cap \Sigma^i$ obtained integrating the flow up to the i -th crossing with the section $\Sigma = \{x = \mu - 1/2\}$ Left: $i = 1$. Middle: $i = 1, 2$. Right: $i = 1, 2, 3$.

3.2.2 Homoclinics of branches of different half-spaces

When taking into account branches of different half-spaces, we can explore the intersection either between W_-^u and W_+^s or between W_+^u and W_-^s . In this Section we have only considered the first case (the other one can be explored analogously). Thus, we consider the matching of W_-^u with W_+^s at the section $\Sigma = \{x = \mu - 1/2\}$, and it is found that first-order homoclinics are of the type $(-1, +4)$. As in the previous section, L_3 does not have a $(-1, +4)$ homoclinic connection, so the curves $W_-^u \cap \Sigma^1$ and $W_+^u \cap \Sigma^4$ do not intersect for energy levels close to h_3 . At energy $h = -1.5004799224$ they become tangent and two families of homoclinics appear. As energy increases the curve $W_+^u \cap \Sigma^4$ winds itself up, in such a way that for energy $h = -1.500476742438758$ there are 28 families of connections (see Fig. 17).

As the branches W_-^u and W_+^s are symmetric with respect to $\tilde{\Sigma} = \{y = 0\}$, a more convenient way to display the intersection of the manifold tubes giving rise to these families of connections is to consider this section (compare

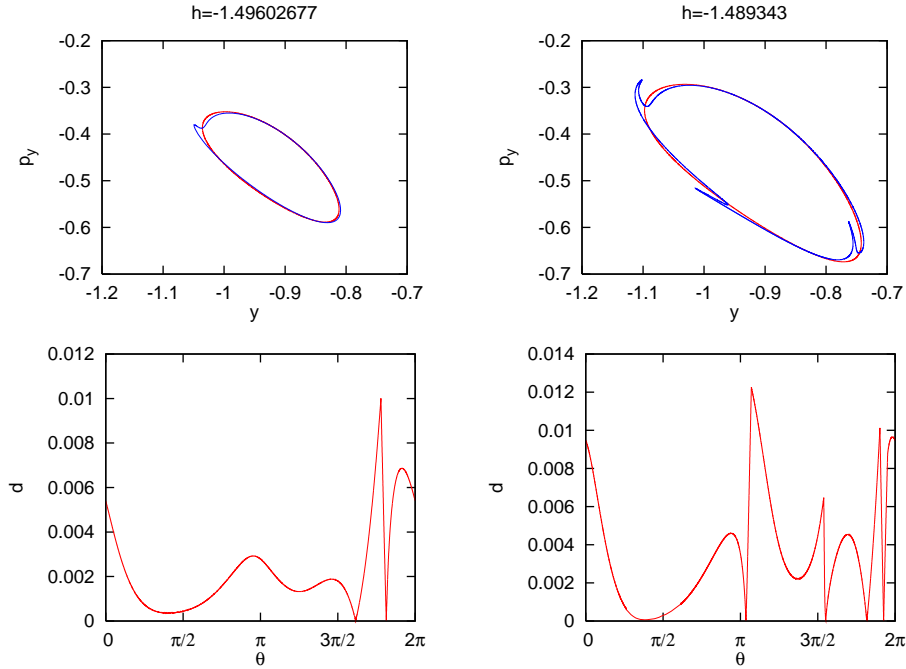


Figure 15: Top: for $\mu = \mu_{SJ}$ and the energies indicated, (y, p_y) projection of curves $W_-^u \cap \Sigma^1$ (red) and $W_-^s \cap \Sigma^2$ (blue). Bottom: The function distance d of each point of the curve $W_-^u \cap \Sigma^1$ to the curve $W_-^s \cap \Sigma^2$, which shows the number of intersections between them.

Figs (17) and (18)). Moreover, in the section $\tilde{\Sigma}$, we can distinguish between symmetric and non-symmetric homoclinics with respect to the symmetry (3). When considering $\tilde{\Sigma}$, symmetric homoclinics are given by the intersection points of the $W_-^u \cap \tilde{\Sigma}^1$ and $W_+^u \cap \tilde{\Sigma}^1$ curves that have $p_x = 0$ ($p_x = 0$ implies $\dot{x} = 0$, since $y = 0$ in $\tilde{\Sigma}$), and the remaining intersection points correspond to non-symmetric homoclinics. With this new section, the families of first-order homoclinics we are considering are of type $(-1, +1)$. Recall that, for each non-symmetric homoclinic, the application of symmetry (3) gives a different connection of the same type.

Let us describe what happens to the curve $W_-^u \cap \tilde{\Sigma}^1$ when the energy increases (see Fig. 18). Notice that $W_+^s \cap \tilde{\Sigma}^1$ can be obtained using the symmetry (3). For $h = -1.50047692243$, both curves become tangent at $y = p_x = 0$ and as h increases, there appear two families of symmetric homoclinic orbits plus two families of non-symmetric ones (see Fig. 18, top

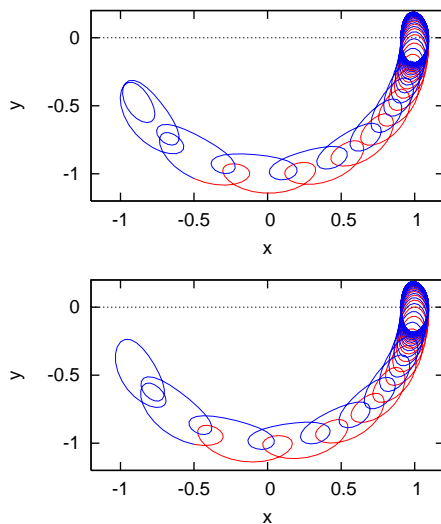


Figure 16: For $\mu = \mu_{SJ}$ and $h = -1.49602677$, projection in configuration space of the two homoclinic orbits found for this energy (see Fig. 15).

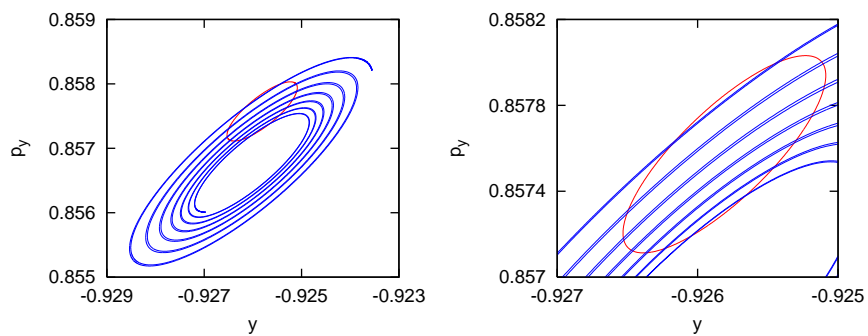


Figure 17: Left: for $\mu = \mu_{SJ}$ and $h = -1.500476742438758$, (y, p_y) projection of the curves $W_-^u \cap \Sigma^1$ (red) and $W_+^s \cap \Sigma^4$ (blue) with $\Sigma = \{x = \mu - 1/2\}$. Right: zoom of the left plot.

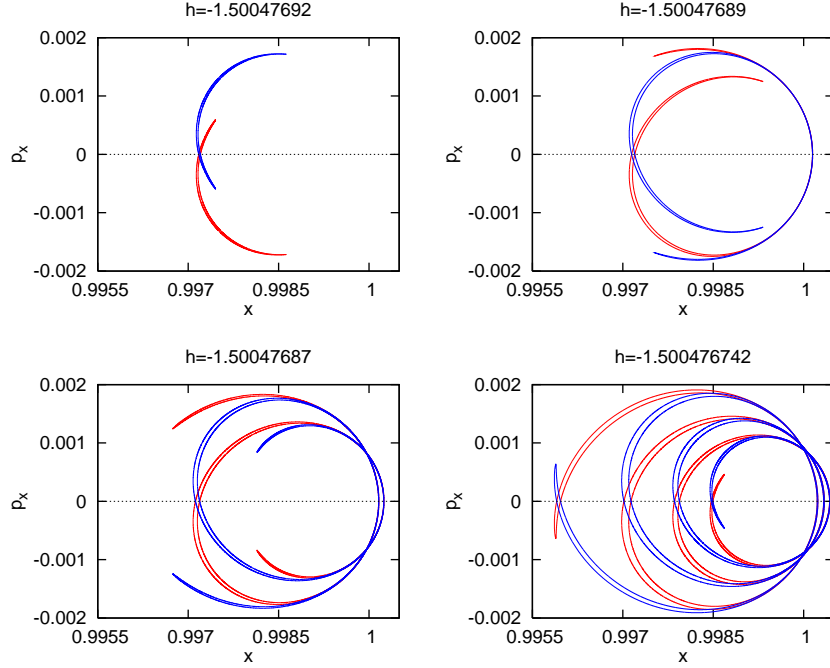


Figure 18: For $\mu = \mu_{S,J}$, projection in the (x, p_x) plane of the sets $W_-^u \cap \tilde{\Sigma}^1$ (red) and $W_+^s \cap \tilde{\Sigma}^1$ (blue) for different values of the energy.

left). For $h = -1.500047691243$ there is a new tangency, so two new families appear (see Fig. 18, top right). As energy increases and approaches the h_t value of Sect. 3.2.1 (the energy value for which first-order homoclinics on the same half space $\{y < 0\}$ are born), new families appear and the curve $W_-^u \cap \tilde{\Sigma}^1$ becomes more intricate (see Fig. 18 bottom right). For $h > h_t$, the set $W_-^u \cap \tilde{\Sigma}^1$ presents a more complicated structure (see Fig. 19). The appearance, for $h > h_t$, of families of first-order homoclinics of branches of the same half-space studied in the previous Section is responsible for this fact. The role that those homoclinics play in the geometry of the successive intersections of W_-^u with $\tilde{\Sigma}^1$ will be clarified in the following Section.

As an example of families of homoclinics of branches on different half spaces, we have continued the 6 families of symmetric homoclinic connections that can be observed in Fig. 18, bottom left. We label such families by Hs_j , $j = 1, \dots, 6$, and their characteristic curves are shown in Fig. 13 right.

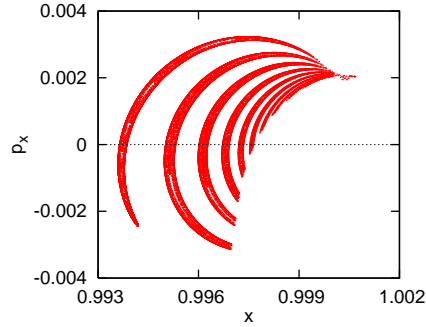


Figure 19: For $\mu = \mu_{SJ}$ and $h = -1.50047477$, projection of part of the set $W_-^u \cap \tilde{\Sigma}^1$ in the (x, p_x) plane (each point of the curve that crosses the $p_x = 0$ axis, corresponds to a symmetric homoclinic orbit of type $(-1, +1)$).

3.2.3 The geometry of the manifold tubes

In this subsection we would like to make some comments on the geometry of manifold tubes for the L_3 case, using the terminology of transit and non-transit orbits introduced in [11]. We would also like to illustrate the appearance of infinite higher-order homoclinics. Similar studies for the L_1 and L_2 points can be found in previous works [19, 21, 27].

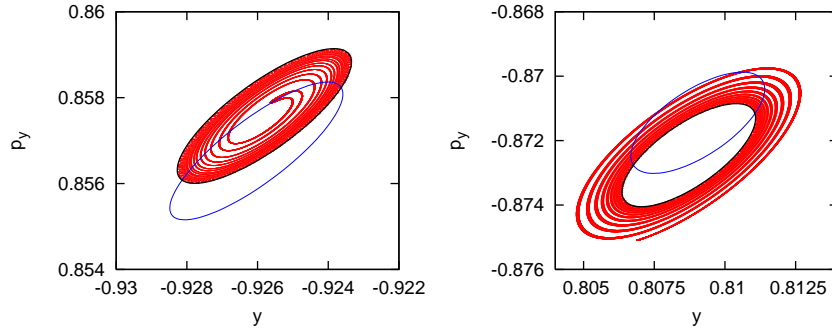


Figure 20: For $\mu = \mu_{SJ}$ and $h = -1.50047477$. Left, (y, p_x) projection of the curves $W_-^s \cap \Sigma^2$ (blue), and the component with $y < 0$ of the curve $W_-^u \cap \Sigma^3$ (red) which spirals tending to the curve $W_-^u \cap \Sigma^1$ (black). Right: (y, p_x) projection of the curves $W_+^s \cap \Sigma^2$ (blue) and the component with $y > 0$ of the curve $W_-^u \cap \Sigma^3$ (red) which spirals tending to the curve $W_+^u \cap \Sigma^1$ (black).

Consider the two homoclinic connections for energy level $h = -1.50047477$ of the families of Fig. 13 left, and the first intersection of the manifold tube

W_-^u with the tube W_-^s in the section $\Sigma = \{x = \mu - 1/2\}$, which gives rise to the $W_-^u \cap \Sigma^1$ and $W_-^s \cap \Sigma^2$ curves. Both curves intersect at two points that correspond to the two homoclinics (see the closed S^1 -like curves in Fig. 20 left). Next, we follow the W_-^u branch up to its 3rd intersection with Σ . The set $W_-^u \cap \Sigma^3$ (shown in Fig. 20) breaks into two parts (one in $\{y < 0\}$ and the other in $\{y > 0\}$), and exhibits a more complicated geometry.

Observe that, fixed this energy level and the sign of \dot{y} , any point in the plane (y, p_x) represented in Fig. 20 uniquely determines a trajectory. Any point not in $W_-^s \cap \Sigma^2$, when propagated forward in time, cannot cross the W_-^s manifold tube. Therefore, any point of Fig. 20 in the interior (bounded) component of the $W_-^s \cap \Sigma^2$ curve will approach the LPO when propagated forward in time. A point outside this curve but close to it will also approach the LPO.

The behavior of trajectories that go close a LPO around L_3 (actually around L_i , for $i = 1, 2, 3$) has been described in [11]. The analysis done in this reference is based on the linear approximation of the flow around the equilibrium point, so it is valid in principle for energies close to the one of L_3 . The numerical experiments below exhibit an analogous behavior for higher energy levels.

According to [11], depending on whether a trajectory is inside or outside (and near) the W_-^s manifold tube, we have the following two possibilities for the next close passage to the LPO forward in time:

- Trajectories inside the W_-^s tube are transit trajectories, in the sense that, for energy levels close to L_3 , they make a transit through the neck region determined by the zero velocity curves. Roughly speaking, they 'cross' the equilibrium region. These trajectories can be obtained starting from an initial condition in Σ such that its projection in the (y, p_x) plane is inside the curve $W_-^s \cap \Sigma^2$ (Fig. 20 left). When followed forward in time, they are close to W_-^s branch, surround the Hill's region (going from one side to the other one), approach the W_-^u branch and remain in the same half-space $\{y < 0\}$ (except perhaps when they are close to the Lyapunov orbit). See Fig. 21, left.
- Trajectories outside (and near) the W_-^s tube are non-transit trajectories. Therefore, these trajectories, when started on the section Σ and followed forward in time, go from the $\{y < 0\}$ half-space to the $\{y > 0\}$ one, approaching the LPO close to the W_-^s branch, and leaving it near the W_+^u one. See Fig. 21 right.

The concept of 'transit or non-transit' is only valid for a specific interval

of time, essentially between consecutive passages close to the LPO. Depending on whether the suitable intersection with Σ lies inside or outside the $W_-^s \cap \Sigma^2$ set, the orbit will have or not a passage through the neck.

With respect to the W_-^u tube, we have a similar situation. When propagated backwards in time, orbits inside the tube remain in the $\{y < 0\}$ region, whereas orbits outside go from $\{y < 0\}$ to $\{y > 0\}$.

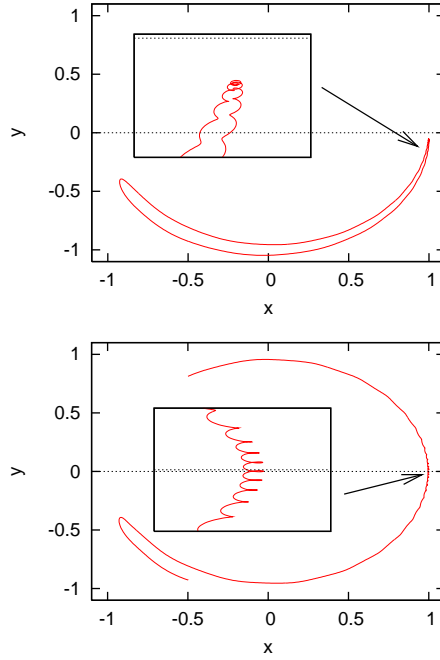


Figure 21: For $\mu = \mu_{SJ}$ and $h = -1.50047477$, examples of a transit (left) and non-transit (right) orbits. See the text for more details.

We consider now the $W_-^u \cap \Sigma^1$ curve (Fig. 20 left) which is divided into two components by the curve $W_-^s \cap \Sigma^2$. According to the concept of transit and non-transit orbits explained above, we can predict the behavior of the orbits on the branch W_-^u when we follow them until the third intersection with Σ :

- The component of $W_-^u \cap \Sigma^1$ inside $W_-^s \cap \Sigma^2$, this is, inside the W_-^s manifold tube, is made of transit orbits. These orbits, when propagated forward in time, come back to the section Σ into the $\{y < 0\}$ region after a close passage to the LPO. Its intersection with Σ is part of the set $W_-^u \cap \Sigma^3$, and is the spiral curve represented in Fig. 20 left.

The points of the starting segment close to any of the two homoclinic connections approach the Lyapunov orbit close to the W_-^s tube and leave it close to the W_-^u tube, therefore accumulating to the $W_-^u \cap \Sigma^1$ curve. They accumulate inside the W_-^u tube, since they come from the $\{y < 0\}$ region and therefore are transit orbits backward in time. Thus, the intersection of this component of the $W_-^u \cap \Sigma^3$ curve with $W_-^s \cap \Sigma^2$ gives rise to an infinity of second-order homoclinics.

- The component of $W_-^u \cap \Sigma^1$ outside the W_-^s manifold tube is made of non-transit orbits, and therefore goes to the $\{y > 0\}$ region when propagated forward in time. The points close to the homoclinic connections accumulate to the $W_+^u \cap \Sigma^1$ curve from outside, since they come from the $\{y < 0\}$ region and therefore are non-transit orbits backward in time. The intersection of this component of $W_-^u \cap \Sigma^3$ with $W_+^s \cap \Sigma^2$ gives rise also to another infinity of second-order homoclinics (see Fig. 20 right).

The existence of transit and non-transit orbits (due to the existence of homoclinic half-horseshoe shaped connections of first order) on the W_-^u tube is the explanation for the complexity shown in Fig. 19, where its first intersection with the section $\tilde{\Sigma} = \{y = 0\}$ is considered. As explained above, one piece of the tube is made of transit orbits (see Fig. 22, left), another piece is made of non-transit orbits (see Fig. 22, right), and an infinity of second-order homoclinics are born (of the two classes: half and full horseshoe shaped). In particular, all the points in Fig. 20 with $p_x = 0$ correspond to symmetric homoclinic connections.

The situation can be iterated. In Fig. 23 we have added $W_-^u \cap \Sigma^5$ to the curves of Fig. 20 left. In the former figure, we can distinguish two pieces of the new $W_-^u \cap \Sigma^5$ curve.

- The piece outside $W_-^u \cap \Sigma^1$ consists of orbits that do not make a transit backward in time. Therefore, they come from the $\{y > 0\}$ region. Since they were started following the W_-^u branch, we can assure that, forward in time, they started in the $\{y < 0\}$ region, after a passage close to the Lyapunov orbit went to the $\{y > 0\}$ region, and after a new LPO passage ended up in the $\{y < 0\}$ region.
- The piece inside $W_-^u \cap \Sigma^1$ corresponds to orbits that come from the $\{y < 0\}$ region. Therefore, they have made two close passages to the LPO never leaving the $\{y < 0\}$ region (except, perhaps, when close to the LPO).

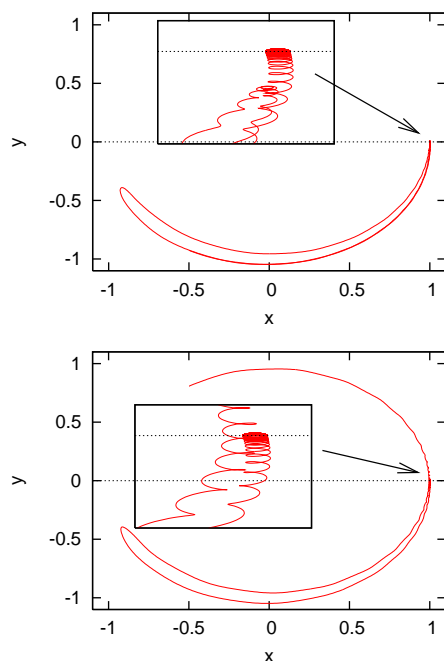


Figure 22: For $\mu = \mu_{SJ}$ and $h = -1.50047477$, projection in configuration space of two different orbits (transit on the left, non-transit on the right) on the same branch W_-^u up to their third intersection with Σ .

The intersection of the $W_-^u \cap \Sigma^5$ curve with $W_-^s \cap \Sigma^2$ gives rise to an infinity of third-order homoclinics.

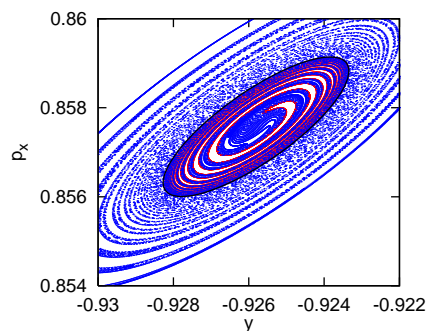


Figure 23: For $\mu = \mu_{SJ}$ and $h = -1.50047477$, (y, p_x) projection of curves $W_-^u \cap \Sigma^1$ (black), $W_-^u \cap \Sigma^3$ (red) and $W_-^u \cap \Sigma^5$ (blue).

Let us consider the set of initial conditions such that its projection in the (y, p_x) plane corresponds to the bounded region Ω limited by $W_-^u \cap \Sigma^1$ in the $\{y < 0\}$ region. The interior of Ω is divided into two components, R_1 and R_2 , by the curve $W_-^u \cap \Sigma^3$ (see Fig. 20, left). By continuity, one of the components, for example R_1 , contains the part of $W_-^u \cap \Sigma^5$ that lies in the interior of Ω (see Fig. 23). We consider the trajectories with initial conditions in R_1 going backward in time. Due to the fact that they are in the interior of Ω as the curve $W_-^u \cap \Sigma^3$, they are transit orbits at the first close passage to the LPO. Furthermore, as they are in the same component than $W_-^u \cap \Sigma^5$, they are also transit orbits in the second close passage to the LPO. So, we know that the points in R_1 , are two times transit orbits backward in time. Using the same reasoning, the points in R_2 are transit orbits in their first passage close to the LPO, but they must come back to the Σ section outside Ω . Thus, they are non-transit in their second passage close to the LPO, and must go to the $\{y > 0\}$ region (always backward in time). In this way, the ‘past’ history of a point inside Ω can be known, up to close encounters with the LPO, from the knowledge of its position with respect the sets $W_-^u \cap \Sigma^{2n+1}$. In the same spirit, the ‘future’ history of these trajectories can be known from the knowledge of their position with respect the intersections $W^s \cap \Sigma^{2n}$.

A rigorous study using symbolic dynamics would allow to show the existence of orbits with prescribed itineraries. Studies of this kind have been done in [19, 21, 30] for LPO around the L_1 and L_2 points. The difference between L_3 and the previous points is that, instead of prescribing itineraries between the interior and exterior regions of the zero velocity curve, here we would prescribe itineraries alternating between the $\{y > 0\}$ and $\{y < 0\}$ regions. Among these trajectories, we could find periodic orbits with half or full horseshoe shape, visiting the upper and lower half-spaces as many times as desired.

4 Acknowledgements

E. Barrabés and J.M. Mondelo are partially supported by the MCyT/FEDER grants BFM2003-09504-C02-01 and MTM2006-05849/Consolider. J.M. Mondelo is also supported by the MCyT/FEDER grant MTM2005-02139. M. Ollé is partially supported by the MCyT/FEDER grant MTM2006-00478.

References

- [1] E. L. ALLGOWER AND K. GEORG, *Numerical continuation methods*, vol. 13 of Springer Series in Computational Mathematics, Springer-Verlag, Berlin, 1990. An introduction.
- [2] E. ANDERSON, Z. BAI, C. BISCHOF, S. BLACKFORD, S. J. DEMMEL, J. DONGARRA, J. D. CROZ, A. GREENBAUM, S. HAMMARLING, A. MCKENNEY, AND D. SORENSEN, *LAPACK Users' Guide*, SIAM, third ed., 1999.
- [3] E. BARRABÉS AND S. MIKKOLA, *Families of periodic horseshoe orbits in the restricted three-body problem*, *Astronomy & Astrophysics*, 432 (2005), pp. 1115–1129.
- [4] E. BARRABÉS AND M. OLLÉ, *Invariant manifolds of l_3 and horseshoe motion in the restricted three-body problem*, *Nonlinearity*, 19 (2006), pp. 2065–2089.
- [5] W.J. BEYN AND J.M. KLEINKAUF, *The numerical computation of homoclinic orbits for maps*, *SIAM J. Numer. Anal.*, 34 (1997), pp. 1207–1236.
- [6] G. D. BIRKHOFF, *Nouvelles recherches sur les systèmes dynamiques.*, *Mem. Pontif. Acad. Sci. Novi Lyncaei*, III. Ser., 1 (1936), pp. 85–216.
- [7] E. CANALIAS, A. DELSHAMS, J. MASDEMONT, AND P. ROLDAN, *The scattering map in the planar restricted three body problem.*, *Cel. Mech Dynam. Astron.*, 95 (2006), pp. 155–171.
- [8] E. CANALIAS AND J. J. MASDEMONT, *Homoclinic and heteroclinic transfer trajectories between planar Lyapunov orbits in the sun-earth and earth-moon systems*, *Discrete Contin. Dyn. Syst.*, 14 (2006), pp. 261–279.
- [9] J. CASOLIVA, J.M. MONDELO, B.F. VILLAC, K.O. MEASE, E. BARRABÉS, M. OLLÉ, *Families of Cycler Trajectories in the Earth–Moon system*, Paper AIAA 2008–6434, AIAA/AAS Astrodynamics Specialist Conference and Exhibit, August 2008, Honolulu, Hawaii.
- [10] A.R. CHAMPNEYS, G.J. LORD, *Computation of homoclinic solutions to periodic orbits in a reduced water-weave problem*, *Phys. D*, 102 (1997), pp. 101–124

- [11] C. C. CONLEY, *Low energy transit orbits in the restricted three-body problem*, SIAM J. Appl. Math., 16 (1968), pp. 732–746.
- [12] M. CONNORS, P. CHODAS, S. MIKKOLA, P. WIEGERT, C. VEILLET, AND K. INNANEN, *Discovery of an asteroid and quasi-satellite in an earth-like horseshoe orbit*, Meteoritics & Planetary Science, 37 (2002), pp. 1435–1441.
- [13] L. DIECI AND J. REBAZA, *Point-to-periodic and periodic-to-periodic connections*, BIT Numer. Math., 44 (2004), pp. 41–62.
- [14] D. W. D. W. DUNHAM AND R. W. FARQUHAR, *Libration point missions, 1978–2002*, in Libration Point Orbits and Applications, G. Gómez, M. W. Lo, and J. J. Masdemont, eds., 2003.
- [15] E. J. DOEDEL, B. W. KOOI, Y. A. KUZNETSOV, AND G. A. K. VAN VOORN, *Continuation of connecting orbits in 3d-odes: (ii) cycle-to-cycle connections*, arXiv:0804.0179v1, (2008).
- [16] E. J. DOEDEL, A. R. CHAMPNEYS, T. F. FAIRGRIEVE, AND Y. A. KUZNETSOV, *Auto97: Continuation and bifurcation software for ordinary differential equations*, tech. report, Concordia University, Montreal, Canada, 1997.
- [17] E. J. DOEDEL, V. A. ROMANOV, R. C. PAFFENROTH, H. B. KELLER, D. J. DICHMANN, J. GALÁN-VIOQUE, AND A. VANDERBAUWHEDE, *Elemental periodic orbits associated with the libration points in the circular restricted 3-body problem*, Internat. J. Bifur. Chaos Appl. Sci. Engrg., 17 (2007), pp. 2625–2677.
- [18] A. FARRÉS, *Stability regions around the Lagrangian points in the RTBP and their boundaries*, master’s thesis, Universitat de Barcelona, 2005.
- [19] M. GIDEA AND J. J. MASDEMONT, *Geometry of homoclinic connections in a planar circular restricted three-body problem*, Internat. J. Bifur. Chaos Appl. Sci. Engrg., 17 (2007), pp. 1151–1169.
- [20] G. GÓMEZ, À. JORBA, J. MASDEMONT, AND C. SIMÓ, *Dynamics and Mission Design Near Libration Point Orbits – Volume 4: Advanced Methods for Triangular Points*, World Scientific, 2001. Reprint of ESA Report *Study of Poincaré Maps for Orbits Near Lagrangian Points*, 1993.

- [21] G. GÓMEZ, W. S. KOON, M. W. LO, J. E. MARSDEN, J. MASDEMONT, AND S. D. ROSS, *Connecting orbits and invariant manifolds in the spatial Restricted Three-Body Problem*, *Nonlinearity*, 17 (2004), pp. 1571–1606.
- [22] G. GÓMEZ, M. MARCOTE, AND J. M. MONDELO, *The invariant manifold structure of the spatial Hill’s problem*, *Dynamical Systems. An International Journal*, 20 (2005), pp. 115–147.
- [23] G. GÓMEZ AND J. J. MASDEMONT, *Some zero cost transfers between Libration Point orbits*, *Advances in the Astronautical Sciences*, 105 (2000), pp. 1199–1216.
- [24] G. GÓMEZ AND J. M. MONDELO, *The dynamics around the collinear equilibrium points of the RTBP*, *Phys. D*, 157 (2001), pp. 283–321.
- [25] K. C. HOWELL, B. T. BARDEN, R. S. WILSON, AND M. W. LO, *Trajectory design using a dynamical systems approach with application to GENESIS*, *Advances in the Astronautical Sciences*, 97 (1998), pp. 1665–1684.
- [26] A. JORBA AND J. MASDEMONT, *Dynamics in the center manifold of the collinear points of the restricted three body problem*, *Physica D*, 132 (1999), pp. 189–213.
- [27] W. S. KOON, M. W. LO, J. E. MARSDEN, AND S. D. ROSS, *Heteroclinic connections between periodic orbits and resonance transitions in celestial mechanics*, *Chaos*, 10 (2000), pp. 427–469.
- [28] B. KRAUSKOPF AND H. M. OSINGA, *Computing invariant manifolds via the continuation of orbit segments*, in *Numerical continuation methods for dynamical systems*, Underst. Complex Syst., Springer, Dordrecht, 2007, pp. 117–154.
- [29] B. KRAUSKOPF AND T. RIESS, *A Lin’s method approach to finding and continuing heteroclinic connections involving periodic orbits*, *Nonlinearity*, 21 (2008), pp. 1655–1690.
- [30] J. LLIBRE, R. MARTÍNEZ, AND C. SIMÓ, *Transversality of the invariant manifolds associated to the Lyapunov family of periodic orbits near L_2 in the restricted three-body problem*, *J. Differential Equations*, 58 (1985), pp. 104–156.

- [31] J. LLIBRE AND M. OLLÉ, *The motion of saturn coorbital satellites in the restricted three-body problem*, *Astronomy and Astrophysics*, 378 (2001), pp. 1087–1099.
- [32] R. P. MCGEHEE, *Some homoclinic orbits for the restricted three-body problem*, PhD thesis, University of Wisconsin, 1969.
- [33] K. R. MEYER AND G. R. HALL, *Introduction to Hamiltonian dynamical systems and the N -body problem*, vol. 90 of Applied Mathematical Sciences, Springer-Verlag, New York, 1992.
- [34] J. M. MONDELO, *Contribution to the Study of Fourier Methods for Quasi-Periodic Functions and the Vicinity of the Collinear Libration Points*, PhD thesis, Universitat de Barcelona, 2001.
- [35] J. M. MONDELO, E. BARRABÉS, G. GÓMEZ, AND M. OLLÉ, *Numerical parametrizations of Libration Point trajectories and their invariant manifolds*, *Advances in the Astronautical Sciences*, 129 (2008), pp. 1153–1168.
- [36] J. MOSER, *Stable and random motions in dynamical systems*, vol. 90 of Applied Mathematical Sciences, Princeton University press, Princeton, New Jersey, 1973.
- [37] J. S. PARKER AND M. W. LO, *Shoot the moon 3D*, *Advances in the Astronautical Sciences*, 123 (2006), pp. 2067–2086.
- [38] C. SIMÓ, *Boundaries of stability*. talk given at Univ. de Barcelona, Jun 3. Available at maia.ub.edu/dsg/, 2006.
- [39] V. SZEBEHELY, *Theory of Orbits. The Restricted Problem of Three Bodies.*, Academic Press, Inc., 1967.
- [40] D. WILCZAK AND P. ZGLICZYŃSKI, *Heteroclinic connections between periodic orbits in planar restricted circular three-body problem—a computer assisted proof*, *Comm. Math. Phys.*, 234 (2003), pp. 37–75.
- [41] ———, *Heteroclinic connections between periodic orbits in planar restricted circular three body problem. II*, *Comm. Math. Phys.*, 259 (2005), pp. 561–576.
- [42] K. YAGASAKI, *Numerical detection and continuation of homoclinic points and their bifurcations for maps and periodically forced systems*, *Internat. J. Bifur. Chaos Appl. Sci. Engrg.*, 8 (1998), pp. 1617–1627.